



# Inverse design of a vanadium dioxide based dynamic structural color *via* conditional generative adversarial networks

PENG DAI,  KAI SUN, OTTO L. MUSKENS,  C. H. DE GROOT, AND RUOMENG HUANG\* 

*Faculty of Engineering and Physical Sciences, University of Southampton, Southampton, SO17 1BJ, United Kingdom*

\**r.huang@soton.ac.uk*

**Abstract:** Dynamic structural color provides an additional time dimension in contrast to the static one, enriching the information load and functionalities. As a phase change material, vanadium dioxide offers great opportunities to implement dynamic structural color as its insulator-metal transition. Nevertheless, the multiple states also place a barrier to the efficient design of the structure configurations. This work firstly reports the dynamic structural color inverse design of asymmetric Fabry-Pérot cavity through a parameter-based conditional generative adversarial networks approach. The proposed structure attains a gamut as large as 117% of sRGB in the insulator state and can produce a 5% color coverage variation *via* the phase change of VO<sub>2</sub> layer. By using the trained conditional generative adversarial networks, the inverse design accuracy with the average color difference  $\Delta E$  of 0.98 is achieved. A monochromatic pattern is designed by the trained networks to demonstrate different color dynamics of the various structures.

Published by Optica Publishing Group under the terms of the [Creative Commons Attribution 4.0 License](#). Further distribution of this work must maintain attribution to the author(s) and the published article's title, journal citation, and DOI.

## 1. Introduction

Structural colors arising from optical interference, diffraction, or scattering have gained significant interest from the research community. Compared with the conventional organic pigment-based coloration which is potentially toxic and vulnerable to degradation under longstanding illumination of intense light [1], structural colors have the advantages of high durability, high resolution, and environmental friendliness [2,3]. These excellent properties give rise to several potential applications in color printing [4–8], data encryption [9,10], and color filter [11–14]. Taking advantages of the nano-patterning techniques, such as electron-beam lithography [15] and nano-imprinting lithography [16–18], a number of structural color prototypes have been successfully manufactured based on metallic plasmonic resonances [19–21], dielectric Mie-scattering [22–25], or resonant cavity [26–28]. Normally, once the structure is defined, the presented color cannot be changed. This static nature of structural colors has significantly limited their application. The capability of dynamically modulating the color is advantageous to extend the structure color with the dimension of time and enrich its information capacity and applications [29].

To implement dynamic or tunable structural colors, it is necessary to embed functional materials into the structure. The change of their optical constants under external stimuli can result in a resonant wavelength shift after the structure is defined. One approach to induce the color change is to adjust the optical constant of the material by chemical reactions [29–31] or ion injection and extraction [32–34]. An alternative method is to employ phase change materials (PCMs) whose optical constant can be modulated by voltage or temperature [35,36]. Vanadium dioxide (VO<sub>2</sub>) is a typical correlated electron material. The Mott transition in VO<sub>2</sub> induces a reversible insulator-metal transition (IMT) within 100 fs at 68°C, which can prominently affect its optical

and electronic properties [37]. Hence, VO<sub>2</sub> is widely used in dynamic spectral modulations, such as infrared absorbers [38–40], and structural colors [37,41–44].

Typical nanophotonic design is usually carried out by sweeping structure parameters in an ample design space *via* numerical simulations to attain a specific structure [45]. Identifying a satisfactory design requires designers with rich experiences and prior physical knowledge [46]. Additionally, the growth of structure complexity would consume vast computation resources, which could prohibitively slow down the iteration period [47]. The inclusion of the additional dimension of the phase state in the phase change material further aggravates the design difficulty of dynamic structural color. Recently, the applications of deep learning (DL) technology in the design of nanophotonic structures have experienced significant development. DL is a technique of machine learning inspired by the neural network of the brain. After applying iterative training processes, the DL model, comprised of artificial neural networks (ANN), can be optimized to fit a function [48]. Owing to its design speed and computation efficiency, numerous works have been reported in which ANNs were utilized to inversely design the structure configurations of different nanophotonic devices for desired optical responses [49–52]. The tandem network is a commonly used DL model in the nanophotonic inverse design [45,53]. It circumvents the “one-to-many” characteristic of most photonics designs by allowing direct comparison in the physical domain. However, the tandem network still suffers a drawback termed *dead zone* where some solutions and solution spaces are unreachable or discarded during the ANN training process [46,54,55]. This problem is caused by the inherent conflicts between the ANN “one-to-one” mapping nature and the inverse design “one-to-many” requirement. To fully tackle this “one-to-many” problem, we recently developed an approach based on conditional generative adversarial networks (cGAN) to the parameter-based inverse design [56]. By introducing the latent vector and distribution shaping ability of cGAN, the dead zone trouble is handled, and one optical response can therefore achieve multiple solutions through cGAN. Furthermore, the design accuracy is improved simultaneously since the cGAN is able to perform searches in the entire solution space which significantly increases the probability of finding the optimal solution.

Here we report, for the first time, an inverse design of reflective dynamic structural color filter *via* cGAN. The structural color filter is realized by an asymmetric Fabry-Pérot (F-P) cavity. Combined with VO<sub>2</sub>, the structural color can be switched by varying the temperature. The proposed F-P cavity covers the gamut as large as 117% of sRGB in the insulative state and obtains 112% sRGB area after the phase transition of VO<sub>2</sub> layer. In order to efficiently predict the structure configuration from demands, we adopt the cGAN model to perform the inverse design. By directly embedding the temperature condition into the inverse task, both VO<sub>2</sub> state design tasks can be executed by a single versatile cGAN. The achieved design accuracy reaches the color difference  $\Delta E_{2000}$  (denoted as  $\Delta E$  below) of 0.98, which exceeds the human eye discernment. The cGAN ability to find multiple solutions is demonstrated by designing an image which is monochromatic at 30°C but shows a distinct pattern when the temperature increases to 85°C. The dynamic structural color inverse design provides a promising approach to find nanophotonic structures to encrypt information and anti-counterfeiting.

## 2. Method

### 2.1. Color prediction module

The color prediction module is comprised of the transfer matrix method (TMM) and the color matching function (CMF). The TMM is used to calculate the spectrum, and the CMF takes the spectrum to obtain the color.

#### Transfer matrix method

The reflective and transmissive spectra of the multilayer structures are calculated *via* the TMM that is provided in Max Born's *Principles of Optics* [57]. The refractive indices of nickel (Ni), silicon dioxide (SiO<sub>2</sub>), and aluminum (Al) are obtained from the *Handbook of Optical Constants*

of Solids by E. D. Palik [58]. The refractive index of titanium dioxide ( $\text{TiO}_2$ ) is extracted from in-house ellipsometry data (Woolam M-2000DI) from a  $\text{TiO}_2$  thin film deposited by a reactive sputtering system (Leybold Helios Pro XL). The refractive indices of  $\text{VO}_2$  at different temperatures are extracted from the work of Kana *et al.* [59]. The detailed calculation equations and processes are provided in [Supplement 1](#), Section 1.

#### Color matching function

The colors in this work are computed by the discrete CIE 1931-XYZ CMF which is provided in *The Science of Color* edited by Steven K. Shevell [60]. After the XYZ tristimulus is obtained, the corresponding CIELAB vector **Lab** is converted from XYZ by the transformation equations in Shevell's work. The detailed equations of the CIE 1931-XYZ color matching function and equations between CIEXYZ and CIELAB are in [Supplement 1](#), Section 1.

## 2.2. Deep learning

### Dataset generation

The thickness combinations in the dataset are uniformly sampled by the open-source library *Numpy* in the ranges of 0 to 1,000 nm for  $\text{TiO}_2$  ( $d_1$ ), 0-20 nm for Ni ( $d_2$ ), 0-500 nm for  $\text{VO}_2$  ( $d_3$ ), and 0-500 nm  $\text{SiO}_2$  ( $d_4$ ). Before applying the thickness sampling, the random seed is fixed as 42 to ensure repeatability. The sampled thickness combinations are then computed to achieve the reflective spectra through the TMM, which will be converted to the CIELAB vectors by the CMF.

### Artificial neural network training

The ANN training loss functions, training processes, and hyperparameters are discussed in [Supplement 1](#), Section 3.

### Image design and reconstruction

The image reconstruction in this work is first converted to a grayscale image. The 50% threshold is applied to binarize the grayscale image. The pixel with the value of 1 in the binary image is set to fill with the background color, and the pixel with the value of 0 in the image is filled with the pattern color.

### Computation environment

The deep learning is implemented on the open-source library *PyTorch*. The dataset preprocessing is executed by *Scikit-Learn*. The color calculations are fished by *Colour-Science*. ANN training and testing programs are developed and performed on a Windows PC with the hardware of CPU: Intel Core i7-11800H, RAM: 32 GB, and GPU: NVIDIA RTX 3080 (16GB).

## 3. Results and discussion

The reflective dynamic structural color filter schematic is illustrated in Fig. 1(a). This thin-film structure consists of a  $\text{TiO}_2/\text{Ni}/\text{VO}_2/\text{SiO}_2/\text{Al}$  stack. The Al layer is fixed at 100 nm at the bottom and serves as a back reflector due to its high reflectivity. The lossless  $\text{SiO}_2$  layer is adopted as a spacer layer to form an asymmetric Fabry-Pérot (F-P) cavity. The dynamic property of the structure is enabled by the phase change material  $\text{VO}_2$ , which is sandwiched by  $\text{SiO}_2$  and Ni. When the temperature changes from 30°C to 85°C, the  $\text{VO}_2$  layer will undergo a lattice transformation from insulative to metallic state, resulting in a variation of its refractive index (as shown in Fig. S1). This variation causes a shift in the F-P resonant wavelength and leads to the change of color. The Ni layer serves as an absorption layer and the top semi-transparent reflector of the F-P cavity to tailor the reflective spectrum. A layer of  $\text{TiO}_2$  covers the top of the multilayer structure as an anti-reflection layer to extend the color gamut. The proposed multilayer structure can be represented by the thicknesses of  $\text{TiO}_2/\text{Ni}/\text{VO}_2/\text{SiO}_2$ , which are denoted as  $d_1$ ,  $d_2$ ,  $d_3$ , and  $d_4$  for  $\text{TiO}_2$ , Ni,  $\text{VO}_2$ , and  $\text{SiO}_2$ , respectively, or as a brief single design vector **D**. Figure 1(b) shows the color change of the proposed structure with the design of (100, 5, 100, 100) nm. The reflective spectrum while  $\text{VO}_2$  at 30°C has two reflective peaks at the wavelengths of ~500 and ~700 nm, respectively. At a higher temperature of 85°C, the peaks blue-shifts to ~480 and ~640

nm. The peak at  $\sim 480$  nm also has an intensity decay due to the  $\text{VO}_2$  phase change. These shifts of peaks are accompanied by a clear change of its color from cyan to pink (shown in the inserts of Fig. 1(b)). This example proves that the proposed  $\text{VO}_2$  based F-P cavity structure can realize the temperature-induced dynamic structure color.

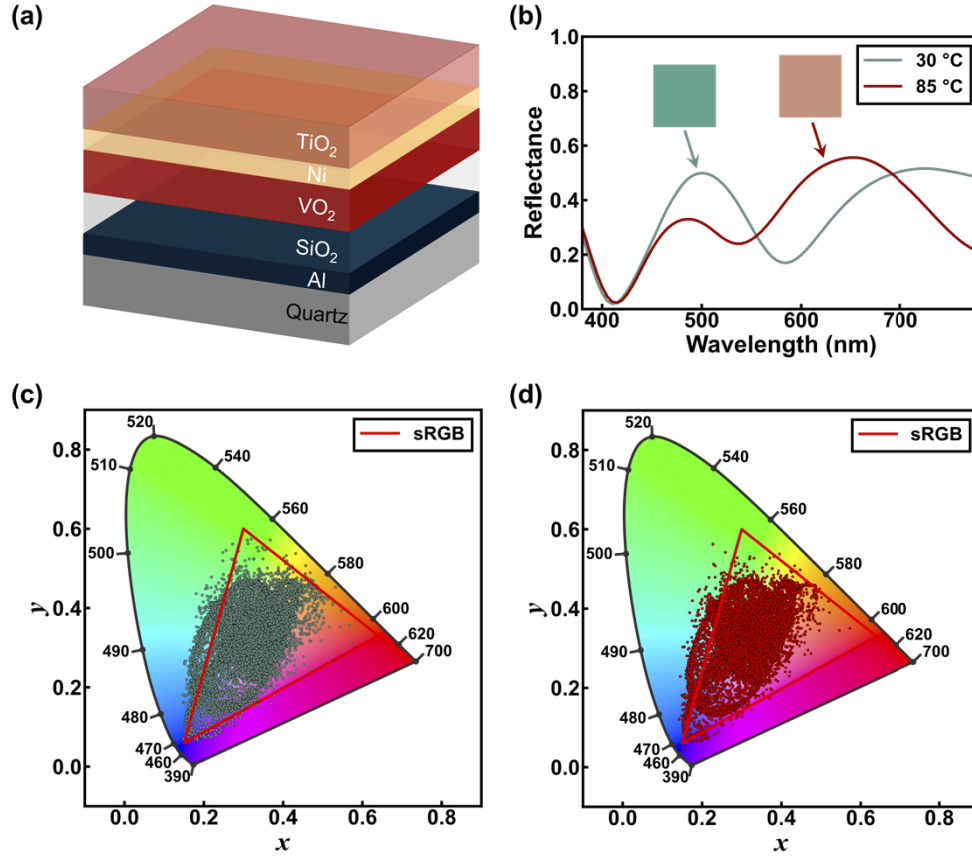


**Fig. 1.** (a) The schematic of the proposed five-layer structure. (b) The reflective spectra of the structure with the thickness of  $\mathbf{D}$  (100, 5, 100, 100) nm at 30 °C (cyan curve) and 85 °C (red curve), in which the inserts are the corresponding colors. (c, d) The CIE 1931-xy chromaticity diagrams of the dataset at 30 °C (c) and 85 °C (d), respectively.

To implement the dynamic structural color inverse design, a dataset with 50,000 samples is generated. 50,000 different  $\text{TiO}_2/\text{Ni}/\text{VO}_2/\text{SiO}_2$  thickness combinations are uniformly sampled from the ranges of 0 to 1,000 nm for  $d_1$  ( $\text{TiO}_2$ ), 0 to 20 nm for  $d_2$  ( $\text{Ni}$ ), and 0 to 500 nm for both  $d_3$  ( $\text{VO}_2$ ) and  $d_4$  ( $\text{SiO}_2$ ). These thickness combinations ( $\mathbf{D}$ s) were then input to the TMM to calculate the reflective spectra, which were fed to the CMF to acquire the corresponding CIELAB coordinates ( $\mathbf{L}$ abs) and CIE 1931-xy chromaticity diagrams. Among the 50,000 samples, 25,000 were converted to colors at 30 °C while the other 25,000 combinations were converted at 85 °C. The obtained color gamuts at 30 °C and 85 °C are shown in Figs. 1(c) and 1(d), demonstrating a color coverage area of 117% and 112% of the sRGB, respectively. The obtained dataset is split into three groups with a ratio of 8:1:1 for training, validation, and testing, respectively.

The inverse design of the dynamic structural color presented in this work is implemented by a cGAN. A common cGAN usually consists of two parts, a generator, and a discriminator. The generator is fed with a latent vector ( $\mathbf{z}$ ) and a condition. The output of the generator is known as

generated data (also called fake data). The discriminator evaluates the distribution difference between the dataset (termed real data) and the generated data (fake data). The training of the discriminator shapes the fake data distribution close to the real data. Owing to the randomness of the latent vector and the discriminator's ability of distribution control, the generator can produce multiple structure designs across the entire solution space [56]. This architecture was adopted and modified in this work to allow the incorporation of temperature. Figure 2(a) provides the cGAN architecture and data flow in this work. The networks have three parts: a generator, a discriminator, and a color prediction module (CPM). To adopt the inverse task going to take place at 30°C and 85°C, the color (**Lab**) and temperature (T) are simultaneously fed into the generator as conditions. The temperature condition is realized by digitalizing the low temperature (30°C) as 0 and the high temperature (85°C) as 1. The latent vector **z** is sampled from the standard normal distribution. The generator is comprised of a residual connected multilayer perceptron (MLP). In the data flow of the generator, the conditions (**Lab** and T) are embedded into the generator *via* the conditional batch normalization layers, and the latent vector is directly fed into the generator which generates the fake thickness as output. In contrast, the discriminator consists of a residual connected MLP with the normal 1-dimensional batch normalization layer. The discriminator separately takes the real and fake thicknesses and outputs the corresponding real and fake scores to measure the distribution distance between real thicknesses and fake thicknesses. In order to improve the generator inverse design accuracy, we used the CPM to predict the color but not a neural network. This module is carried out by the TMM and the CMF. The TMM taking fake thickness and temperature outputs the reflective spectrum to the CMF to acquire the predicted **Lab**. The introduction of CPM can predict the color of the structure without deviation to improve the performance of the generator. The CPM used in this work is fully developed with *PyTorch* to ensure that the color prediction process is differentiable. The implementation details of the generator, the discriminator, and the CPM are available in [Supplement 1](#), Section 2.

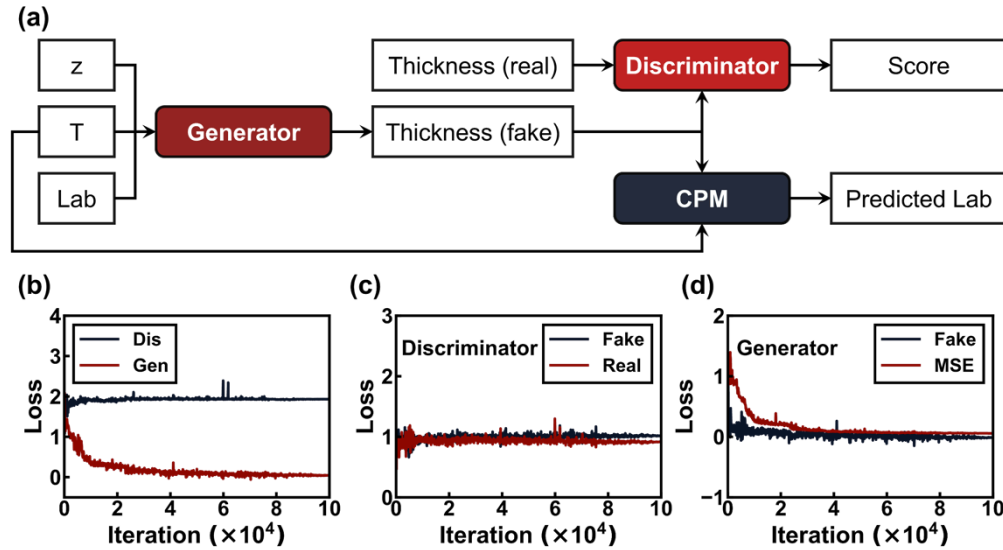


**Fig. 2.** (a) The data flow and the cGAN architecture in this work. (b) The loss curves of the discriminator (black curve) and the generator (red curve). (c) The components of discriminator loss, where the black curve is the fake score and the red curve is the real score. (d) The components of generator loss, where the black curve is the fake score, the red curve is the MSE which is computed between the input **Lab** and predicted **Lab** in Fig. 2(a).



To keep the training stability of the cGAN, the Wasserstein distance is utilized as the distribution loss [61]. The spectral normalization is applied to both the generator and the discriminator ensuring the 1-Lipschitz continuity [62]. The generator and the discriminator are alternatively updated with the step ratio of 1:1 to minimize the hinge adversarial loss by two Adam optimizers [63]. The detailed training hyperparameters and loss functions can be seen in Supplement 1, Section 3. The training loss curves of the generator and the discriminator are displayed in Fig. 2(b). The discriminator loss is steadily *ca.* 2 after an initial fluctuation. This indicates the cGAN experienced a stable training process. The evolution of discriminator fake and real scores as the iterations can be seen in Fig. 2(c). Both the fake score and the real score of the discriminator were maintained at around 1 over the entire training process, indicating that the generator and the discriminator are evenly improved. This is crucial to the performance of the generator [56]. Figure 2(d) presents the loss details of the generator. The small fluctuation of the generator's fake score around the 0 translates into a stable generator evolution, and no model collapse happened during the training process. The continuous descending mean squared error (MSE) in Fig. 2(d) is computed between the **Lab** predicted by the CPM and the ground truth **Lab**. After a fast drop in the first 10,000 iterations, the MSE practices a slow decline and finally bottoms at *ca.*  $4.9 \times 10^{-2}$ , reflecting that generator's prediction accuracy improved quickly and then gradually converged.

The dynamic structural color inverse design accuracy benchmark is represented by the color difference index  $\Delta E$  between the trained generator's predictions and the ground truths in the testing set. The meaning of  $\Delta E$  is described in Ref. [64]. Typically, it is considered that no color difference is perceived by the human eye when  $\Delta E < 1$ . In the testing process, the colors (**Labs**) from the testing set and the latent vector (**z**) sampled from the standard normal distribution are fed to the generator to predict the fake thicknesses. The fake thicknesses are taken into the CPM to calculate the predicted **Lab**. The  $\Delta E$  calculation function is applied to calculate the color difference between the predicted **Lab** and the ground truth **Lab** to identify the design bias. The testing  $\Delta E$  histogram when each **Lab** is assigned with one **z** is shown in Fig. 3(a). Almost all  $\Delta E$  are found to be less than 10 with an average  $\Delta E$  of 4.86. This can be easily improved by increasing the number of **z** for each **Lab** to generate different **D** combinations for selection. Figure 3(b) presents the histogram of  $\Delta E$  when the number of **z** for each **Lab** was increased to 1,000. By selecting the best design (lowest  $\Delta E$ ) from the 1,000 designs, the majority of  $\Delta E$  is found to be below 1. The average  $\Delta E$  for all 5,000 samples is 0.98, which is beyond the human eye's color resolution, reflecting a satisfactory inverse design accuracy. Figure 3(c) illustrates the average lowest  $\Delta E$  in the testing set as the function of the **z** number of each **Lab**. As the increase of **z** number, the average  $\Delta E$  initially drops drastically (insert presents the enlargement of the yellow shading area) and breaks the threshold of 1 when the **z** number exceeds 1,000. Afterward, the design accuracy gains limited improvement with the **z** number growth. It is worth mentioning that increasing the **z** number is straightforward and largely effortless. For example, applying inverse design and solution selection for 5,000 colors with 1,000 **z** sampling for each color will only consume 38.82 s in our computation environment, which is equivalent to 7.76 ms per color. Additionally, the CPM (non-ANN part) costs 6 ms during the solution selected from 1,000 candidates and occupies 77.3% time consumption of a color inverse design, indicating that the ANN only spends a small proportion of the wall-clock time and shows a high computation efficiency. In this work, a **z** number of 1,000 was subsequently adopted for all designs to balance both the performance and computational time.

To better evaluate the performance of our network, we selected four colors that the network has never seen before. The eight target colors shown in Fig. 3(d) were fed into our network with their corresponding temperatures and 1,000 **z** to generate and select designs with the lowest  $\Delta E$ . The designs were subsequently converted to colors and compared with their targets. It can be

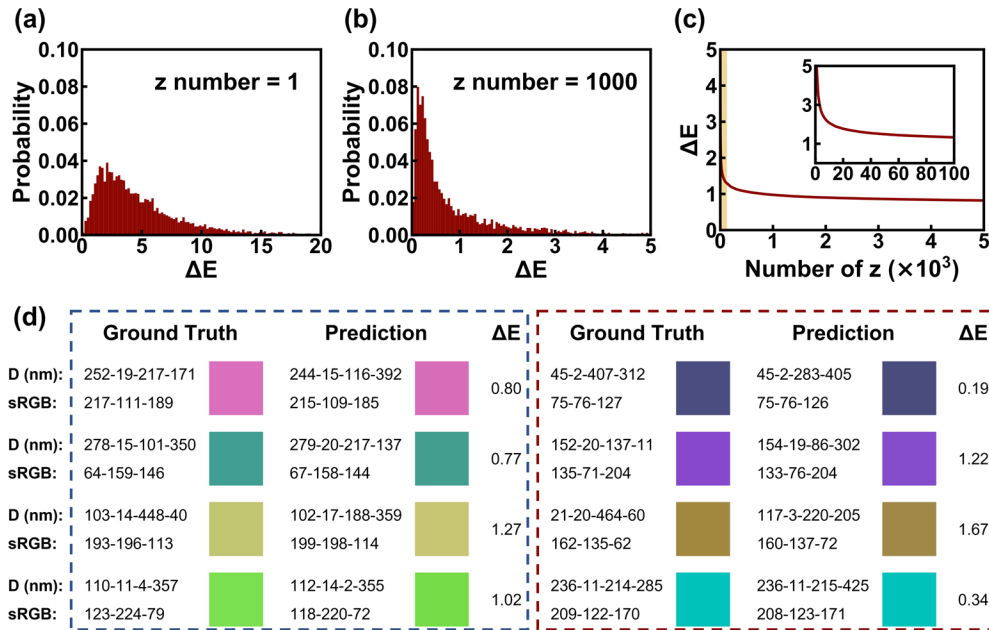






















**Fig. 3.** (a, b) The testing  $\Delta E$  histograms when each **Lab** is assigned with 1 **z** (a) and 1,000 **z** (b), respectively. (c) The testing average  $\Delta E$  as the function of the number of **z**, in which the insert is the enlargement of the yellow shading region. (d) Eight cGAN inverse design examples, the target colors with 30°C are outlined by a blue dash frame (left), and the target colors with 85°C are outlined by a red dash frame (right).

observed that our network was able to predict structural colors that are very close to the original target for both high and low temperature scenarios.

The key performance indicator of the five-layer stack is the color change performance. Here we define a dynamic  $\Delta E_D$  to evaluate the color difference between the low and high temperatures of one design. A larger  $\Delta E_D$  is more advantageous to demonstrate the color modulation capability. Taking advantage of the cGAN developed in this work, we are able to identify the design that gives rise to the largest  $\Delta E_D$  for each color. As a demonstration, we selected five colors in the low temperature region from the testing set. For each color, we generated 1,000 different solutions by feeding 1,000 **z** to the generator. The design with the lowest  $\Delta E$  and the largest  $\Delta E_D$  of each color is listed in Table 1, in which the solution with the lowest  $\Delta E$  is referred to as accurate (ACC) solution, and the solution with the largest  $\Delta E_D$  is termed dynamic (DYN) solution. The color cells are shaded with the corresponding colors. Significant color variances can be observed between the low temperature and high temperature scenarios with that the DYN  $\Delta E_D$  over 20 is obtained for all six colors in the DYN solutions. This clearly demonstrates the capability of our structure to color modulation. It should be noted that selecting the structures with the largest  $\Delta E_D$  compromises the design accuracy as the most color dynamic structures may not always be the most precise design. As an example, the DYN solution of sample #4 shows a large  $\Delta E_D$  of 39.89 where totally different colors were observed at 30°C and 85°C. However, the  $\Delta E$  of this DYN solution ( $\Delta E = 4.71$ ) is inferior to that of the ACC solution ( $\Delta E = 0.28$ ). It is evident that the capability of our network in identifying multiple solutions enables the selection of designs that suits different requirements, e.g. temperature indication.

To demonstrate the potential application, we used the cGAN to design the logo of the University of Southampton (raw image shown in Fig. S4(a)). The designed pattern structure has

Table 1. The Inverse Design Examples with Temperature Induced Color Variation

True <b>D</b> (nm)	True Color (30°C)	DYN Solution (nm)	DYN Color		DYN		ACC Solution (nm)	ACC Color		ACC	
			30°C	85°C	$\Delta E$	$\Delta E_D$		30°C	85°C	$\Delta E$	$\Delta E_D$
227-1-302-334	157-136-130	946-4-123-160			2.01	22.74	944-1-135-137			0.26	19.27
163-15-104-29	0-103-201	46-15-46-218			2.70	23.14	46-15-46-218			2.70	23.14
329-14-383-152	170-171-168	82-3-96-5			6.58	25.67	92-4-197-5			3.92	13.96
133-2-364-248	162-106-114	47-0-124-16			4.71	39.89	133-2-270-100			0.28	11.84
127-11-124-46	180-152-110	197-0-87-41			0.43	24.58	197-0-87-41			0.43	24.58

a configuration of **D** (83, 4, 96, 125) nm, which fills in the pixels of the logo. The background is set as a design with the **D** of (87, 6, 129, 163) nm. The designed logo shows as light blue when the temperature is 30°C (Fig. 4(a)) but appears pink after the temperature rises to 85°C (Fig. 4(b)), while concurrently the background changes from gray to green, demonstrating a large contrast between the two images.

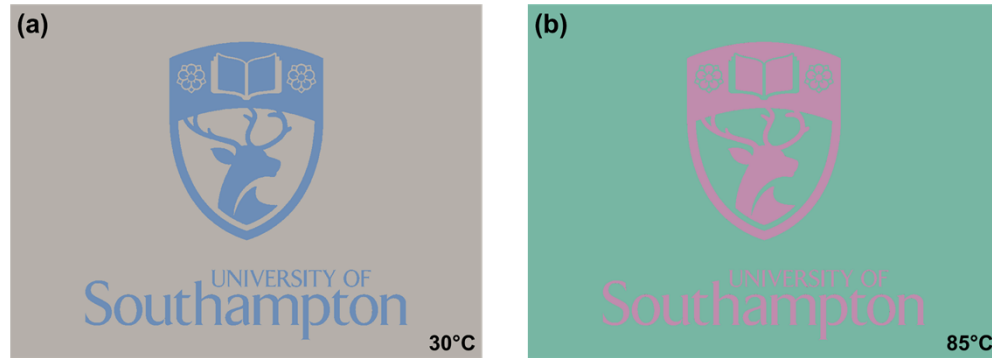


**Fig. 4.** (a) The cGAN inverse designed University of Southampton logo at 30°C. (b) The same image at 85°C.

Potentially more interestingly, the capability of identifying multiple solutions for each color allows the design of a pattern with undistinguishable colors at one temperature but drastic color contrast at another. As an example, we selected a color with the sRGB value of (198-127-149) as the design target. The color was fed to the generator with 1,000 **z** at 30°C to produce 1,000 solutions. Two solutions, that are similar at low temperature but have good contrast at high temperature, are chosen. The obtained two solutions have the structures of: solution 1 **D**<sub>1</sub> (481, 2, 44, 186) nm with the  $\Delta E$  of 0.97 and the  $\Delta E_D$  of 6.32; solution 2 **D**<sub>2</sub> (237, 4, 143, 91) nm with the  $\Delta E$  of 2.11 and the  $\Delta E_D$  of 12.50. The spectra and corresponding colors of solutions 1 and 2 are displayed in Figs. 5(a) and 5(b). Solution 1 has 6 resonant peaks, while solution 2 only has 2, but they present a very similar color at 30°C, which proves the “one-to-many” mapping nature of this five-layer stack inverse design and that our cGAN demonstrates a great ability to find multiple solutions. The target reproduction pattern is taken from a photo of the University of Southampton Highfield campus. The photo is converted to a grayscale image, then, binarized by the 50% threshold. The binary pattern is shown in Fig. S4(b). During the reproduction, the white pixels are filled with solution 1, and the black pixels are filled with solution 2. The



reproduced pattern results are shown in Figs. 5(c) and 5(d). It is impossible to find a pattern in Fig. 5(c), and only a monochromatic pink blank is observed. Whereas a clear binary map with the sign of “University of Southampton”, buildings and other features can be clearly seen at 85°C. Fig. S5 presents another set of designs that shows the similar effect. This highlights the unique advantages of our cGAN in designing dynamic structural colors and points toward its applications in data encryption and anti-counterfeiting, etc.

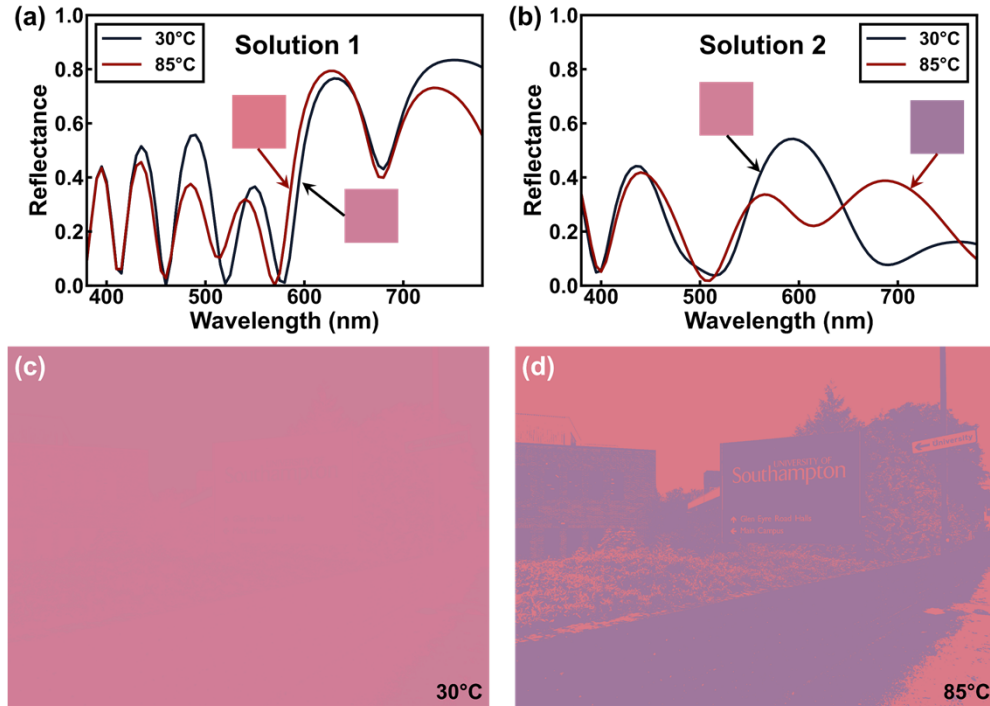


**Fig. 5.** The spectra of (a) solution 1 and (b) solution 2, where the inserts are the corresponding colors of the spectra. The reproduced campus photo at 30°C (c) and at 85°C (d).

#### 4. Conclusion

In conclusion, we demonstrate the inverse design of VO<sub>2</sub> based dynamic structural color *via* cGAN. The proposed F-P cavity structure has a gamut that is 117% gamut area of sRGB and is capable of dynamically modulating color when the temperature changes from 30°C to 85°C. After training, the cGAN can produce structure designs for both temperatures with an average color difference  $\Delta E$  as small as 0.98 when sampling 1,000  $\mathbf{z}$  for each color. In addition, the capability of generating multiple design solutions for one target color enables the identification of designs that allows the largest dynamic color change between the two temperatures. This dynamic structural color design has the potential to encode spatial information by selecting designs showing indiscernible color differences at one temperature but a large difference at another. The VO<sub>2</sub> based structural color design allows the ability to control color dynamically and the unique capability of inverse design of its structures *via* our cGAN can significantly boost its applications in data encryption and anti-counterfeiting.

**Funding.** Engineering and Physical Sciences Research Council (EP/N035437/1).

**Acknowledgments.** This work is a part of the ADEPT project funded by a program grant from the Engineering and Physical Sciences Research Council (EP/N035437/1).

**Disclosures.** The authors declare no conflicts of interest.

**Data availability.** Data underlying the results presented in this paper are available in Ref. [65].

**Supplemental document.** See [Supplement 1](#) for supporting content.

## References

1. C. Yang, W. Shen, Y. Zhang, K. Li, X. Fang, X. Zhang, and X. Liu, "Compact multilayer film structure for angle insensitive color filtering," *Sci. Rep.* **5**(1), 9285 (2015).
2. S. Daqiqeh Rezaei, Z. Dong, J. You En Chan, J. Trisno, R. J. H. Ng, Q. Ruan, C.-W. Qiu, N. A. Mortensen, and J. K. W. Yang, "Nanophotonic structural colors," *ACS Photonics* **8**(1), 18–33 (2021).
3. Z. Xuan, J. Li, Q. Liu, F. Yi, S. Wang, and W. Lu, "Artificial structural colors and applications," *The Innovation* **2**(1), 100081 (2021).
4. K. Kumar, H. Duan, R. S. Hegde, S. C. W. Koh, J. N. Wei, and J. K. W. Yang, "Printing colour at the optical diffraction limit," *Nat. Nanotechnol.* **7**(9), 557–561 (2012).
5. X. Zhu, W. Yan, U. Levy, N. A. Mortensen, and A. Kristensen, "Resonant laser printing of structural colors on high-index dielectric metasurfaces," *Sci. Adv.* **3**(5), e1602487 (2017).
6. Y. Wang, M. Zheng, Q. Ruan, Y. Zhou, Y. Chen, P. Dai, Z. Yang, Z. Lin, Y. Long, and Y. Li, "Stepwise-nanocavity-assisted transmissive color filter array microprints," *Research* **2018**, (2018).
7. X. Zhu, C. Vannahme, E. Højlund-Nielsen, N. A. Mortensen, and A. Kristensen, "Plasmonic colour laser printing," *Nat. Nanotechnol.* **11**(4), 325–329 (2016).
8. Z. Yang, Y. Chen, Y. Zhou, Y. Wang, P. Dai, X. Zhu, and H. Duan, "Microscopic interference full-color printing using grayscale-patterned Fabry–Perot resonance cavities," *Adv. Opt. Mater.* **5**(10), 1700029 (2017).
9. Z. Li, A. W. Clark, and J. M. Cooper, "Dual Color Plasmonic Pixels Create a Polarization Controlled Nano Color Palette," *ACS Nano* **10**(1), 492–498 (2016).
10. J. Xue, Z.-K. Zhou, Z. Wei, R. Su, J. Lai, J. Li, C. Li, T. Zhang, and X.-H. Wang, "Scalable, full-colour and controllable chromotropic plasmonic printing," *Nat. Commun.* **6**(1), 8906 (2015).
11. S. Yokogawa, S. P. Burgos, and H. A. Atwater, "Plasmonic Color Filters for CMOS Image Sensor Applications," *Nano Lett.* **12**(8), 4349–4354 (2012).
12. K.-T. Lee, S. Y. Han, Z. Li, H. W. Baac, and H. J. Park, "Flexible High-Color-Purity Structural Color Filters Based on a Higher-Order Optical Resonance Suppression," *Sci. Rep.* **9**(1), 14917 (2019).
13. B. Yang, W. Liu, D.-Y. Choi, Z. Li, H. Cheng, J. Tian, and S. Chen, "High-Performance Transmission Structural Colors Generated by Hybrid Metal-Dielectric Metasurfaces," *Adv. Opt. Mater.* **9**(21), 2100895 (2021).
14. B. Yang, W. Liu, Z. Li, H. Cheng, D.-Y. Choi, S. Chen, and J. Tian, "Ultrasaturated Structural Colors Enhanced by Multipolar-Modulated Metasurfaces," *Nano Lett.* **19**(7), 4221–4228 (2019).
15. Z. Dong, L. Jin, S. D. Rezaei, H. Wang, Y. Chen, F. Tjiptoharsono, J. Ho, S. Gorelik, R. J. H. Ng, Q. Ruan, C.-W. Qiu, and J. K. W. Yang, "Schrödinger's red pixel by quasi-bound-states-in-the-continuum," *Sci. Adv.* **8**(8), eabm4512 (2022).
16. Z. Liu, Q. Cui, Z. Huang, and L. J. Guo, "Transparent Colored Display Enabled by Flat Glass Waveguide and Nanoimprinted Multilayer Gratings," *ACS Photonics* **7**(6), 1418–1424 (2020).
17. S. Baek, K. Kim, Y. Sung, P. Jung, S. Ju, W. Kim, S.-J. Kim, S.-H. Hong, and H. Lee, "Solution-processable multi-color printing using UV nanoimprint lithography," *Nanotechnology* **31**(12), 125301 (2020).
18. M. F. Shahin Shahidan, J. Song, T. D. James, and A. Roberts, "Multilevel nanoimprint lithography with a binary mould for plasmonic colour printing," *Nanoscale Adv.* **2**(5), 2177–2184 (2020).
19. S. J. Tan, L. Zhang, D. Zhu, X. M. Goh, Y. M. Wang, K. Kumar, C.-W. Qiu, and J. K. W. Yang, "Plasmonic Color Palettes for Photorealistic Printing with Aluminum Nanostructures," *Nano Lett.* **14**(7), 4023–4029 (2014).
20. F. Cheng, J. Gao, L. Stan, D. Rosenmann, D. Czaplewski, and X. Yang, "Aluminum plasmonic metamaterials for structural color printing," *Opt. Express* **23**(11), 14552–14560 (2015).
21. S. D. Rezaei, R. J. Hong Ng, Z. Dong, J. Ho, E. H. H. Koay, S. Ramakrishna, and J. K. W. Yang, "Wide-Gamut Plasmonic Color Palettes with Constant Subwavelength Resolution," *ACS Nano* **13**(3), 3580–3588 (2019).
22. Z. Dong, J. Ho, Y. F. Yu, Y. H. Fu, R. Paniagua-Dominguez, S. Wang, A. I. Kuznetsov, and J. K. W. Yang, "Printing Beyond sRGB Color Gamut by Mimicking Silicon Nanostructures in Free-Space," *Nano Lett.* **17**(12), 7620–7628 (2017).
23. S. Sun, Z. Zhou, C. Zhang, Y. Gao, Z. Duan, S. Xiao, and Q. Song, "All-Dielectric Full-Color Printing with TiO<sub>2</sub> Metasurfaces," *ACS Nano* **11**(5), 4445–4452 (2017).
24. W. Yang, S. Xiao, Q. Song, Y. Liu, Y. Wu, S. Wang, J. Yu, J. Han, and D.-P. Tsai, "All-dielectric metasurface for high-performance structural color," *Nat. Commun.* **11**(1), 1864 (2020).
25. J. Proust, F. Bedu, B. Gallas, I. Ozerov, and N. Bonod, "All-Dielectric Colored Metasurfaces with Silicon Mie Resonators," *ACS Nano* **10**(8), 7761–7767 (2016).
26. Z. Li, S. Butun, and K. Aydin, "Large-Area, Lithography-Free Super Absorbers and Color Filters at Visible Frequencies Using Ultrathin Metallic Films," *ACS Photonics* **2**(2), 183–188 (2015).
27. J. Zhao, M. Qiu, X. Yu, X. Yang, W. Jin, D. Lei, and Y. Yu, "Defining Deep-Subwavelength-Resolution, Wide-Color-Gamut, and Large-Viewing-Angle Flexible Subtractive Colors with an Ultrathin Asymmetric Fabry–Perot Lossy Cavity," *Adv. Opt. Mater.* **7**(23), 1900646 (2019).

28. M. A. Kats, R. Blanchard, P. Genevet, and F. Capasso, "Nanometre optical coatings based on strong interference effects in highly absorbing media," *Nat. Mater.* **12**(1), 20–24 (2013).
29. Y. Chen, X. Duan, M. Matuschek, Y. Zhou, F. Neubrech, H. Duan, and N. Liu, "Dynamic Color Displays Using Stepwise Cavity Resonators," *Nano Lett.* **17**(9), 5555–5560 (2017).
30. X. Duan, S. Kamin, and N. Liu, "Dynamic plasmonic colour display," *Nat. Commun.* **8**(1), 14606 (2017).
31. X. Duan and N. Liu, "Scanning Plasmonic Color Display," *ACS Nano* **12**(8), 8817–8823 (2018).
32. Y. Lee, J. Yun, M. Seo, S.-J. Kim, J. Oh, C. M. Kang, H.-J. Sun, T. D. Chung, and B. Lee, "Full-Color-Tunable Nanophotonic Device Using Electrochromic Tungsten Trioxide Thin Film," *Nano Lett.* **20**(8), 6084–6090 (2020).
33. M. Huang, A. Jun Tan, F. Büttner, H. Liu, Q. Ruan, W. Hu, C. Mazzoli, S. Wilkins, C. Duan, J. K. W. Yang, and G. S. D. Beach, "Voltage-gated optics and plasmonics enabled by solid-state proton pumping," *Nat. Commun.* **10**(1), 5030 (2019).
34. Z. Wang, X. Wang, S. Cong, J. Chen, H. Sun, Z. Chen, G. Song, F. Geng, Q. Chen, and Z. Zhao, "Towards full-colour tunability of inorganic electrochromic devices using ultracompact fabry-perot nanocavities," *Nat. Commun.* **11**(1), 302 (2020).
35. F. Neubrech, X. Duan, and N. Liu, "Dynamic plasmonic color generation enabled by functional materials," *Sci. Adv.* **6**(36), eabc2709 (2020).
36. K. V. Sreekanth, R. Medwal, Y. K. Srivastava, M. Manjappa, R. S. Rawat, and R. Singh, "Dynamic Color Generation with Electrically Tunable Thin Film Optical Coatings," *Nano Lett.* **21**(23), 10070–10075 (2021).
37. S. Song, X. Ma, M. Pu, X. Li, Y. Guo, P. Gao, and X. Luo, "Tailoring active color rendering and multiband photodetection in a vanadium-dioxide-based metamaterial absorber," *Photonics Res.* **6**(6), 492–497 (2018).
38. L. Lei, F. Lou, K. Tao, H. Huang, X. Cheng, and P. Xu, "Tunable and scalable broadband metamaterial absorber involving VO<sub>2</sub>-based phase transition," *Photonics Res.* **7**(7), 734–741 (2019).
39. K. Sun, C. A. Riedel, A. Urbani, M. Simeoni, S. Mengali, M. Zalkovskij, B. Bilenberg, C. H. de Groot, and O. L. Muskens, "VO<sub>2</sub> Thermochromic Metamaterial-Based Smart Optical Solar Reflector," *ACS Photonics* **5**(6), 2280–2286 (2018).
40. K. Sun, W. Xiao, C. Wheeler, M. Simeoni, A. Urbani, M. Gaspari, S. Mengali, C. H. Kees de Groot, and O. L. Muskens, "VO<sub>2</sub> metasurface smart thermal emitter with high visual transparency for passive radiative cooling regulation in space and terrestrial applications," *Nanophotonics* (2022).
41. J. Zhao, Y. Zhou, Y. Huo, B. Gao, Y. Ma, and Y. Yu, "Flexible dynamic structural color based on an ultrathin asymmetric Fabry-Perot cavity with phase-change material for temperature perception," *Opt. Express* **29**(15), 23273–23281 (2021).
42. K. Wilson, C. A. Marocco, and A. L. Bradley, "Dynamic structural colour using vanadium dioxide thin films," *J. Phys. D: Appl. Phys.* **51**(25), 255101 (2018).
43. X. Duan, S. T. White, Y. Cui, F. Neubrech, Y. Gao, R. F. Haglund, and N. Liu, "Reconfigurable Multistate Optical Systems Enabled by VO<sub>2</sub> Phase Transitions," *ACS Photonics* **7**(11), 2958–2965 (2020).
44. F.-Z. Shu, F.-F. Yu, R.-W. Peng, Y.-Y. Zhu, B. Xiong, R.-H. Fan, Z.-H. Wang, Y. Liu, and M. Wang, "Dynamic Plasmonic Color Generation Based on Phase Transition of Vanadium Dioxide," *Adv. Opt. Mater.* **6**(7), 1700939 (2018).
45. L. Gao, X. Li, D. Liu, L. Wang, and Z. Yu, "A bidirectional deep neural network for accurate silicon color design," *Adv. Mater.* **31**(51), 1905467 (2019).
46. P. R. Wiecha, A. Arbouet, C. Girard, and O. L. Muskens, "Deep learning in nano-photonics: inverse design and beyond," *Photonics Res.* **9**(5), B182–B200 (2021).
47. J. Jiang, D. Sell, S. Hoyer, J. Hickey, J. Yang, and J. A. Fan, "Free-form diffractive metagrating design based on generative adversarial networks," *ACS Nano* **13**(8), 8872–8878 (2019).
48. I. Goodfellow, Y. Bengio, and A. Courville, *Deep Learning* (MIT press, 2016).
49. W. Ma, F. Cheng, and Y. Liu, "Deep-Learning-Enabled On-Demand Design of Chiral Metamaterials," *ACS Nano* **12**(6), 6326–6334 (2018).
50. Z. Liu, D. Zhu, S. P. Rodrigues, K.-T. Lee, and W. Cai, "Generative model for the inverse design of metasurfaces," *Nano Lett.* **18**(10), 6570–6576 (2018).
51. J. Jiang and J. A. Fan, "Global Optimization of Dielectric Metasurfaces Using a Physics-Driven Neural Network," *Nano Lett.* **19**(8), 5366–5372 (2019).
52. F. Wen, J. Jiang, and J. A. Fan, "Robust freeform metasurface design based on progressively growing generative networks," *ACS Photonics* **7**(8), 2098–2104 (2020).
53. D. Liu, Y. Tan, E. Khoram, and Z. Yu, "Training Deep Neural Networks for the Inverse Design of Nanophotonic Structures," *ACS Photonics* **5**(4), 1365–1369 (2018).
54. R. S. Hegde, "Deep learning: a new tool for photonic nanostructure design," *Nanoscale Adv.* **2**(3), 1007–1023 (2020).
55. P. Dai, Y. Wang, Y. Hu, C. de Groot, O. Muskens, H. Duan, and R. Huang, "Accurate inverse design of Fabry-Perot-cavity-based color filters far beyond sRGB via a bidirectional artificial neural network," *Photonics Res.* **9**(5), B236–B246 (2021).
56. P. Dai, K. Sun, X. Yan, O. L. Muskens, C. H. Kees de Groot, X. Zhu, Y. Hu, H. Duan, and R. Huang, "Inverse design of structural color: finding multiple solutions via conditional generative adversarial networks," *Nanophotonics* (2022).

57. M. Born and E. Wolf, *Principles of Optics: Electromagnetic Theory of Propagation, Interference and Diffraction of Light* (Elsevier, 2013).
58. E. D. Palik, *Handbook of Optical Constants of Solids* (Academic Press, 1998), 3.
59. J. B. Kana Kana, J. M. Ndjaka, G. Vignaud, A. Gibaud, and M. Maaza, "Thermally tunable optical constants of vanadium dioxide thin films measured by spectroscopic ellipsometry," *Opt. Commun.* **284**(3), 807–812 (2011).
60. S. K. Shevell, *The Science of Color* (Elsevier, 2003).
61. M. Arjovsky, S. Chintala, and L. Bottou, "Wasserstein Generative Adversarial Networks," in (PMLR, 2017), pp. 214–223.
62. T. Miyato, T. Kataoka, M. Koyama, and Y. Yoshida, "Spectral normalization for generative adversarial networks," ArXiv Prepr. ArXiv180205957 (2018).
63. H. Zhang, I. Goodfellow, D. Metaxas, and A. Odena, "Self-Attention Generative Adversarial Networks," in *Proceedings of the 36th International Conference on Machine Learning*, K. Chaudhuri and R. Salakhutdinov, eds., Proceedings of Machine Learning Research (PMLR, 2019), 97, pp. 7354–7363.
64. W. Mokrzycki and M. Tatol, "Colour difference  $\Delta E$  - A survey," *Mach Graph Vis* **20**(4), 383–411 (2011).
65. P. Dai, K. Sun, O. Muskens, K. de Groot, and R. Huang, "Dataset for Inverse design of vanadium dioxide based dynamic structural color via conditional generative adversarial networks," University of Southampton, 2022, <https://doi.org/10.5258/SOTON/D2295>.